AIAA AVIATION 2017
5-9 Jun 2017, Denver, CO
AIAA-2017-3654

Simultaneous Pressure and Optical Measurements Around Hemispherical Turret in Subsonic and Transonic Flight

Jacob Morrida[1], Nicholas De Lucca[2], Stanislav Gordeyev[3], Eric J. Jumper[4]
University of Notre Dame, Notre Dame, Indiana, 46545

The aero-optical environment and unsteady surface pressure in the wake around a hemispherical turret were experimentally studied in flight between Mach numbers 0.5 and 0.8. Optical wavefronts and surface pressures were collected simultaneously to study the correlation between optically active flow features, like the unsteady shock, over the aperture with pressure at several locations on the surface downstream of the hemisphere. The unsteady shock location statistics were extracted and analyzed from the optical data. The shock was found to have a predominantly upstream motion with associated low frequency of $St_D \sim 0.2$. Two modal decomposition techniques, POD and DMD, were implemented to decompose the wavefronts into orthogonal and dynamic modes. The temporal coefficients from POD and DMD were correlated with the pressures to study the shock effect at transonic speeds on global dynamics of the wake. It was found that the presence of the shock enhances the correlation between the optical distortions and the pressure in the wake in the range of frequencies of $St_D \sim 0.1 - 0.4$.

I. Introduction

A hemispherical turret is a practical geometry for airborne platforms for housing lasers, optical sensors, or airborne telescopes for navigation, weapons, or communication applications. However, using this geometry leads to various aerodynamic effects, including a complex separated wake downstream of the turret, which can negatively impact system performance [1]. At Mach numbers above 0.55, a local supersonic region, with a resulted unsteady shock appears near the apex of the turret [1,2]. At these high transonic speeds, the unsteady shock, due to associated pressure gradients, was observed to start influencing the separated wake [3,4].

Many realistic environment optical measurements have been collected in flight using the AAOL and AAOL-T programs in order to study optical distortions, and the unsteady shock dynamics [5-9]. Still, the exact details of the interaction between the unsteady shock, the related separation wake and the resulted pressure field in the wake are not quite clear. Simultaneous wavefront-pressure measurements on top of a 2-D spanwise-cylinder revealed that they are highly correlated [10], suggesting and a lock-in mechanism between the shock and the wake; some evidence of this lock-in mechanism was observed in flight for hemisphere-on-cylinder turret [3,15]. For the cylindrical turret, these correlations were found to be sufficiently strong to successfully predict the wavefronts using pressure field only [11]. This correlation would be particularly useful for flow control, or adaptive optics applications if the wavefronts can be estimated from non-optical pressure data. For conventional adaptive-optics systems, when applying an adaptive optics control loop to higher frequency application on the order of 1 kHz, latency issues arise associated with measuring and reconstructing instantaneous wavefronts [13,14], so the wavefront reconstruction based on non-optical input is a promising way to avoid the latency issue. Furthermore, using non-optical input for adaptive optics is advantageous, as it does not require a cooperative target to predict the wavefronts [11].

---

[1]Graduate Student, Department of Mechanical and Aerospace Engineering, Hessert Laboratory for Aerospace Research, Notre Dame, IN 46556, Student AIAA Member.

[2] Graduate Student, Department of Mechanical and Aerospace Engineering, Hessert Laboratory for Aerospace Research, Notre Dame, IN 46556, AIAA Student Member

[3]Research Associate Professor, Department of Mechanical and Aerospace Engineering, Hessert Laboratory for Aerospace Research, Notre Dame, IN 46556, AIAA Associate Fellow.

[4]Professor, Department of Mechanical and Aerospace Engineering, Hessert Laboratory for Aerospace Research, Notre Dame, IN 46556, AIAA Fellow.

For the 2-D cylinder pressure sensors were placed along the aperture on the cylinder; for realistic hemispherical turrets it might be difficult to place the pressure sensors by the aperture. Preliminary studies of the wake dynamics downstream of the turret at subsonic and transonic speeds [4,10] had revealed that there is a coupling between the shock and the wake. Utilizing this coupling it might be possible to estimate the instantaneous wavefronts and the shock position from pressure information in the turret wake. This paper will present the results of the recent experiments to collect and study simultaneous wavefronts for the hemispherical turret and unsteady pressure field in multiple points in the wake downstream of the turret.

II. Experimental Setup

Simultaneous optical and pressure measurements were performed during a flight test using the AAOL-T. The AAOL-T program consists of two Falcon 10 aircraft flying in closed formation. The laser aircraft projects a diverging laser beam that overfills the aperture by a factor of 2 onto the turret of the laboratory aircraft, which is equipped with a 12-inch diameter turret with a 4-inch aperture, see Figure 1, left. Aircraft separation is maintained at approximately 50 m while data is being acquired. Wavefront measurements were performed using a high-speed Shack-Hartmann wavefront sensor based on v1611 Phantom camera, shown in Figure 1, right. The sensor featured a lenslet array with 32x32 subapertures. The AAOL-T program, and the instrumentation are described in more detail in [8,15]. One of the primary goals of this experiment was to study the unsteady shock motion near the apex of the turret, so data was collected with the aperture located in the shock region, see Table 1.

The pressure measurements were made with several Kulite pressure transducers mounted to the aircraft surface. One was mounted upstream to acquire incoming pressure fluctuations, while another seven were mounted downstream of the hemisphere in a T-pattern, shown in Figure 1, left. The approximate distances from the center of the hemisphere to each pressure sensor in the streamwise and vertical directions in the plane frame of reference is given in Table 2, and Figure 2 shows the numbers corresponding to each sensor. Note that the local flow is rotated by 6 degrees, relative to the incoming freestream velocity, as indicated in Figure 2, due to the aircraft non-zero angle-of-attack. So, Sensors 1, 2 and 4 are aligned in the streamwise direction along the wake centerline in the local flow frame of reference, and Sensors 3 – 7 are approximately aligned in the spanwise direction in the local flow frame of reference. The sensors' positions were chosen to be inside the recirculation region, with Sensor 3 close to the re-attachment point.

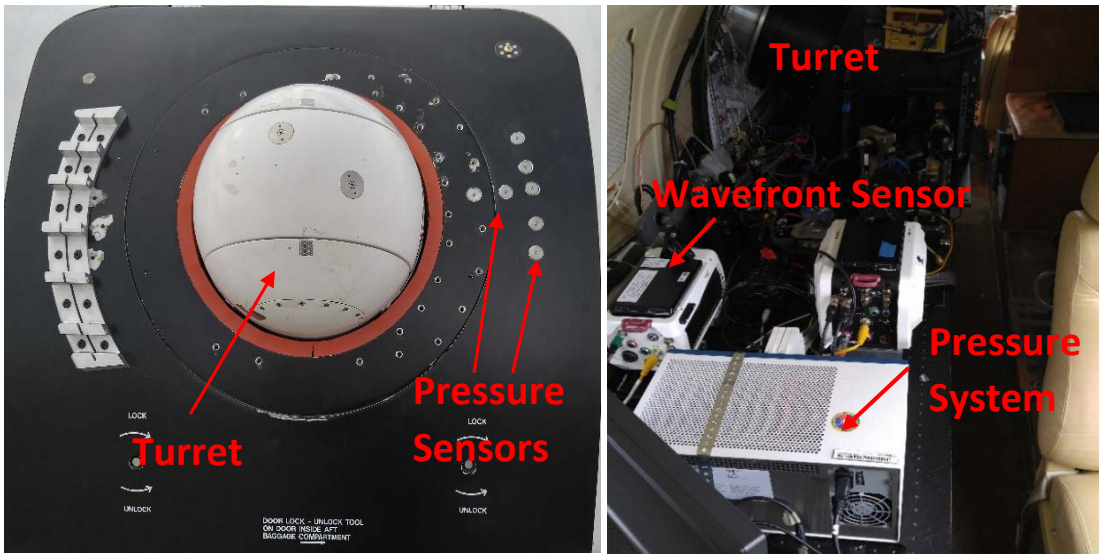

Figure 1. The hemispherical turret and pressure sensors mounted downstream of the turret on the side of Falcon 10 aircraft (left), the optical bench with instrumentation inside the aircraft (right).

Table 1: Azimuth and Elevation Angles of the aperture for each Mach number.

Mach Number	0.5	0.6	0.7	0.8
Azimuth Angle, *Az* (degrees)	105.1	99.6	83.5	98.4
Elevation Angle, *El* (degrees)	59.1	59.1	64.6	69.5

Table 2: Kulite locations for the flight test.

Kulite Number	Downstream Distance from Hemisphere Center (inches)	Downstream Distance Normalized by Diameter	Vertical Distance from Hemisphere Center (inches)
1	7.5	0.63	0.8
2	8.7	0.73	0.9
3	9.6	0.80	-3.5
4	9.9	0.82	-2.1
5	10.1	0.84	1.2
6	10.3	0.86	0.5
7	10.3	0.86	1.7

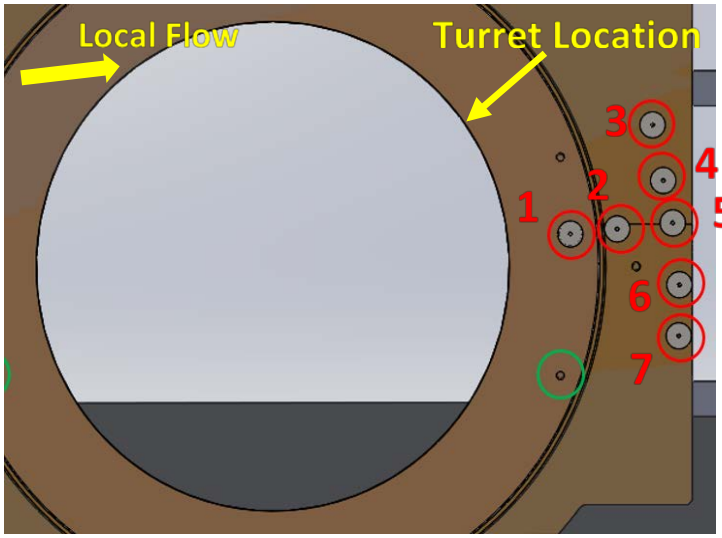

Figure 2: Schematic of pressure sensors in the hemisphere wake for flight tests. Enumerated red circles indicate the Kulite locations. Local flow is rotated upward by 6 degrees relative to the incoming freestream flow.

Measurements at different azimuthal/elevation angles were obtained at M = 0.5-0.6 at an altitude of 14,000 ft and M = 0.7 and 0.8 at 28,000-30,000 ft. Wavefront data was collected for 0.84 seconds and pressure data were collected simultaneously with the wavefront data for 20 seconds, both at a rate of 25 kHz.

III. Data Analysis

The images from Shack-Hartmann high-speed wavefront sensor were reduced using in-house software, to obtain aero-optical distortions, expressed as $OPD(x,y,t)$, as a function of location on the aperture and time. The return beam was flipped and rotated as it travels through the optical setup, so the Shack-Hartmann image must first be oriented so that the vertical and horizontal directions are in the aperture-based frame of reference; this frame of reference was chosen to coincide with elevation and azimuthal angle directions, respectively. Instantaneous piston and tip/tilt were removed from each wavefront by least-squares plane fitting the wavefronts, and steady lensing was removed by subtracting the mean from each wavefront.

To study the shock motion on the hemisphere geometry it is convenient to recast the azimuthal (Az) and elevation (El) angle coordinate system into viewing angle and modified elevation angle [5]. The viewing angle, α, determines how far downstream on the hemisphere the point is and the modified elevation angle, β, defines how far the point is from the plate. The viewing angle is given by $\alpha = \cos^{-1}\left(\cos(Az)\cos(El)\right)$, and the modified elevation angle is given by $\beta = \tan^{-1}\left(\frac{\tan(El)}{\sin(Az)}\right)$. The inverse transformation is given by $EL = \sin^{-1}[\sin(\alpha)\sin(\beta)]$, and $Az = \tan^{-1}[\sin(\alpha)\cos(\beta)/\cos(\alpha)]$. After converting coordinates, 1-D slices of the wavefront were taken at each time

step in the viewing angle direction for fixed β-angles, and the shock location was extracted by finding the point of a maximum positive slope.

Proper orthogonal decomposition (POD) analysis was applied to the wavefronts to decompose them into different modes for the analysis. The POD modes, $\varphi_n(s)$, and mode energies, λ_n, was found by solving the integral equation,

$$\int_S R(s,s')\varphi(s')ds' = \lambda_n\varphi_n(s) \tag{2}$$

The variable R is a time-averaged correlation matrix given by,

$$R(s,s') = \overline{OPD(s,t)OPD(s',t)} \tag{3}$$

where *OPD* is the piton/tilt-removed distortions, *s* is the location on the hemisphere surface, and *t* is time. The aero-optical field can be reconstructed from the POD modes,

$$OPD(s,t) = \sum_n a_n(t)\varphi_n(s) \tag{4}$$

$$a_n(t) = \int_S OPD(s,t)\varphi_n(s)ds, \quad \overline{a_n(t)a_m(t)} = \lambda_n\delta_{nm} \tag{5}$$

The POD modes show the primary flow features, arranged by their energy contribution. This provides a convenient way to study correlations between pressure and optical POD modes.

Dynamic Mode Decomposition was also used to analyze the data. The algorithm used for DMD is outlined in [16,17,18,19]. DMD decomposes the optical distortions, OPD, into spatial modes, φ, eigenvalues, λ, to represent the frequency and exponential decay rate of the modes and amplitudes, c,

$$OPD\left(\vec{x},t\right) \approx \sum_{k=1}^{n} b_k e^{\lambda_k t}\phi_k\left(\vec{x}\right). \tag{6}$$

This is done by breaking the wavefront data set into two sets, OPD_1 and OPD_2. If the data set has N total frames of wavefronts, OPD_1 contains the first N-1 frames and OPD_2 contains the last N-1 frames given by

$$\begin{aligned} OPD_1 &= \{w_1, w_2, \ldots, w_{N-1}\} = V_1 \\ OPD_2 &= \{w_2, w_3, \ldots, w_N\} = V_2 \end{aligned}; \tag{7}$$

Another word, these two data sets are offset by a single time step. The goal is to find a matrix *A* such that the second data set is written as a linear combination of the first data set,

$$OPD_2 = A \cdot OPD_1. \tag{8}$$

This matrix is called the companion matrix. An estimate to it, *S* is determined by

$$V_2 = AV_1 = V_1S - r\,,\; S = \arg\min\left\|V_2 - V_1S\right\| \tag{9}$$

where *r* is the residual. *A* and *S* are similar in that they share the same eigenvalues. The eigenvectors between the two matrices are related as well.

The actual computation of the DMD modes starts with the singular value decomposition (SVD) of the first data set, OPD_1:

$$V_1 = U\Sigma W^H, \tag{10}$$

where the H superscript denotes the Hermitian transpose. The above relationship between OPD_1, OPD_2 and *S*, can have the SVD of the first data set substituted in,

$$\begin{aligned} V_2 &= U\Sigma W^H S \quad \text{and} \\ S &= UV_2\Sigma^{-1}W = U^H AU = Y\mu Y^{-1} \end{aligned} \tag{11}$$

Here μ and Y are the eigenvalues and eigenvectors of the eigenvalue problem of S,

$$SY = \mu Y\,. \tag{12}$$

The DMD modes and eigenvalues can be computed from the eigenvectors and eigenvalues of S by

$$\phi = V_1 Y\ ,\ \lambda = \ln(\mu)/\Delta t\ . \tag{13}$$

The frequency and exponential decay rate of the DMD modes can be found in the eigenvalues. The frequency is given by the imaginary part of the eigenvalue and the decay rate is given by the real part,

$$e^{\lambda_k t} = e^{\mathrm{Re}(\lambda_k)t + i\,\mathrm{Im}(\lambda_k)t}\ . \tag{14}$$

To find the expression for b_k-coefficients in Eq. (6), we can substitute the decomposition of S into the relationship between V_1 and V_2 above,

$$V_2 = V_1 S = V_1 Y \mu Y^{-1} = \phi \mu Y^{-1} = \phi c_k\ ,$$

Here μY^{-1} serves the same role as the temporal coefficients, c_k, of standard POD decomposition,

$$V_2 \equiv OPD_2 = \sum_{k=1}^{N-1} \phi_k c_k(t).$$

These c_k – coefficients are complex and have real and imaginary parts that take the form of decaying or growing sine waves. By comparing this equation with Eq. (6), we get $c_k = b_k e^{\lambda_k t}$. The square of the modulus of $c_k(f)$ is related to the power spectra of OPD. Note that, unlike for POD decomposition, where the eigenmodes are orthogonal, the eigenmodes are not orthogonal for DMD, therefore $OPD_{rms}^2 \neq \sum_{k=1}^{N-1} |c_k(f)|^2$. However for simplicity, later in this paper we will call $|c_k(f)|^2$ as a DMD power spectrum.

IV. Results

Figure 3 shows the spatial-temporal evolution of the shock location on the hemisphere at Mach 0.8. The shock is located where there is a steep positive gradient in OPD. Its strength is proportional to the change in the OPD across the shock (ΔOPD). The shock typically moves between 83 and 87 degrees, with the average location of 85 degrees, and favors locations around 84 and 86 degrees. The shock is not present, or at least has a reduced intensity, at some instances, as seen around T = 4. The motion is not as periodic as it was observed for conformal window hemisphere-on-cylinder turrets at Mach 0.8 [3,15]. This is probably due to a weaker shock, as for the same Mach numbers aero-optical distortions due to the shock are generally smaller for the hemispherical turret than for the hemisphere-on-cylinder turrets [6] .

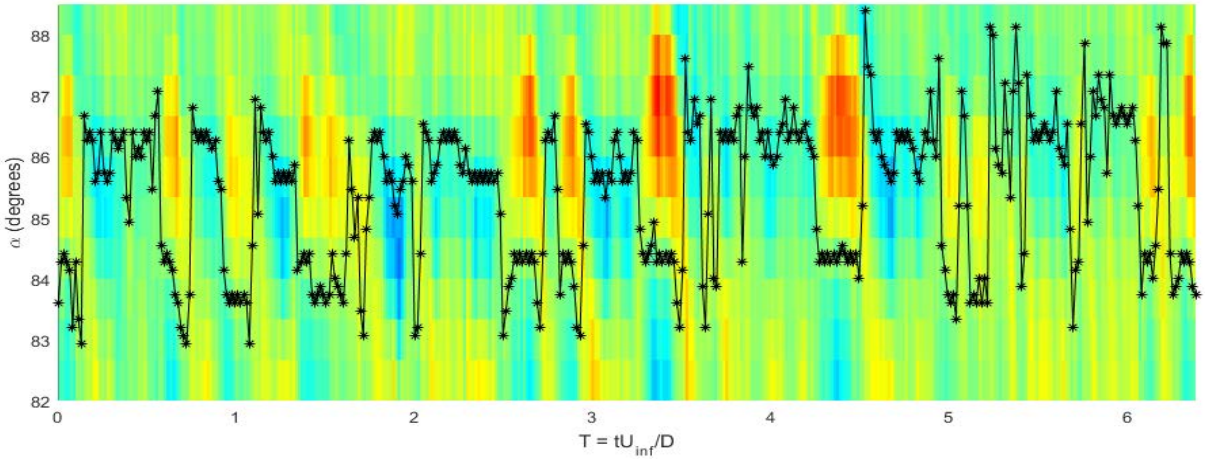

Figure 3: Spatial temporal evolution of the 1-D slices of the wavefronts in α-direction with shock location represented by a black line for Mach 0.8.

A shock is not present on the hemisphere at every time step, so only points with a minimum ΔOPD greater than 30% of the maximum value were counted as a shock. Figure 4 depicts the shock location probability density function.

The mean shock location is around 85 degrees for both Mach numbers and the shock is located between 82 degrees and 88 degrees. The distribution is not Gaussian and has two peaks near α = 83.5 and 86 degrees.

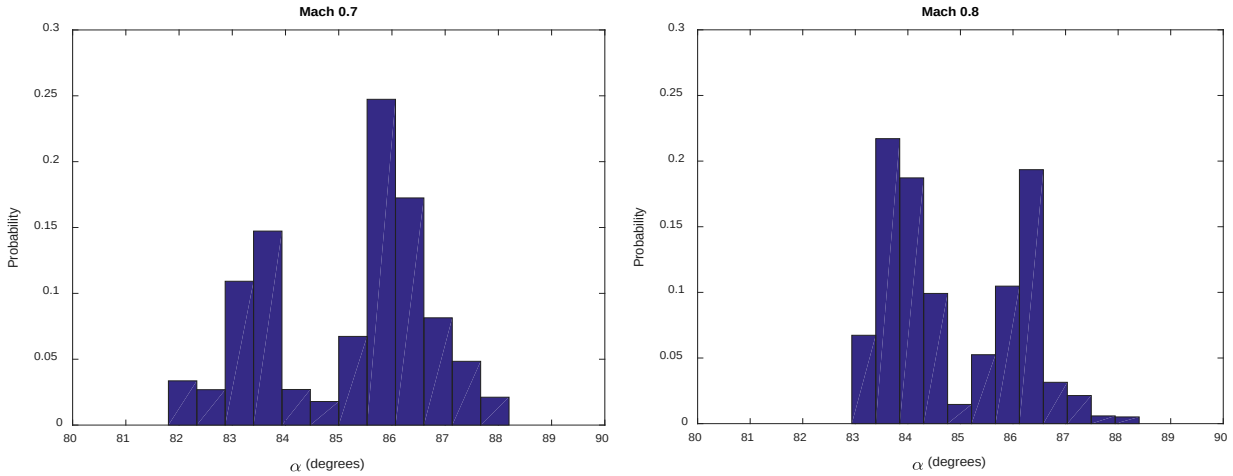

Figure 4: Shock location probability density function for Mach 0.7 (left) and Mach 0.8 (right).

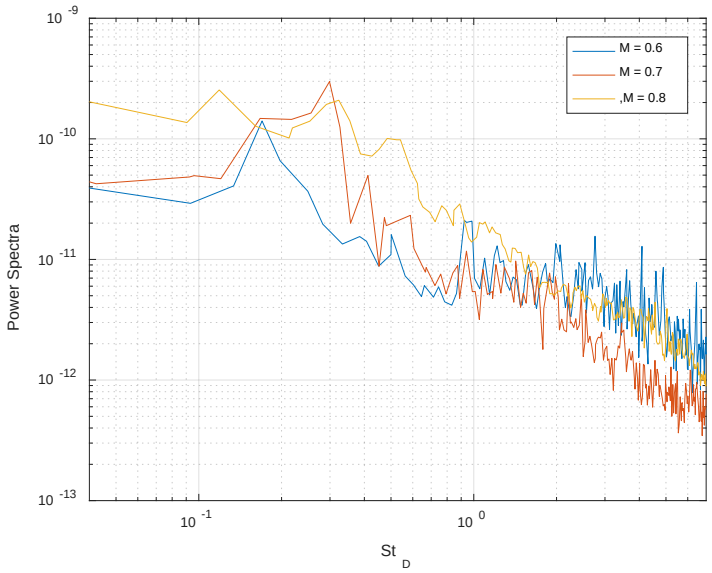

Figure 5: DMD power spectra for Mach 0.6 – 0.8.

Figure 5 shows the DMD power spectra for Mach 0.6 – 0.8. The highest amount of energy at transonic speeds is in the modes at the frequencies $St_D \equiv fD/U_\infty = 0.1..0.3$. This frequency range was associated to the separation over the turret [20]; the unsteady shock was also found to be associated with this frequency range [3,6,7]. Spectra at Mach 0.7 and 0.8 have more energy than Mach 0.6 due to the shock presence. Spectra at Mach 0.7 has a peak around $St_D = 0.3$, whereas the spectrum at Mach 0.8 has one around $St_D = 0.15$. So, at higher Mach numbers the peak in the spectrum shifts to a lower frequency matching the separation line motion [20] when the shock strength is higher. This behavior has also been seen in the shock motion in previous wind tunnel and flight tests [3,6].

Figure 6 shows the real and imaginary parts of the DMD modes for Mach 0.7 and 0.8 near a frequency of $St_D = 0.15$; as mentioned before this associated with the shock motion frequency. The shock is clearly visible in the real and imaginary parts for both Mach numbers as the high gradient region where the color changes from dark blue to yellow or red. At Mach 0.8, the gradient is larger due to the increased shock strength. In the real part the shock does not look symmetric in β-angle direction for either Mach number, indicating that instantaneously the shock is not at a constant α-angle. The imaginary part shows anti-correlation between the shock, seen in blue, and the incoming flow seen as red.

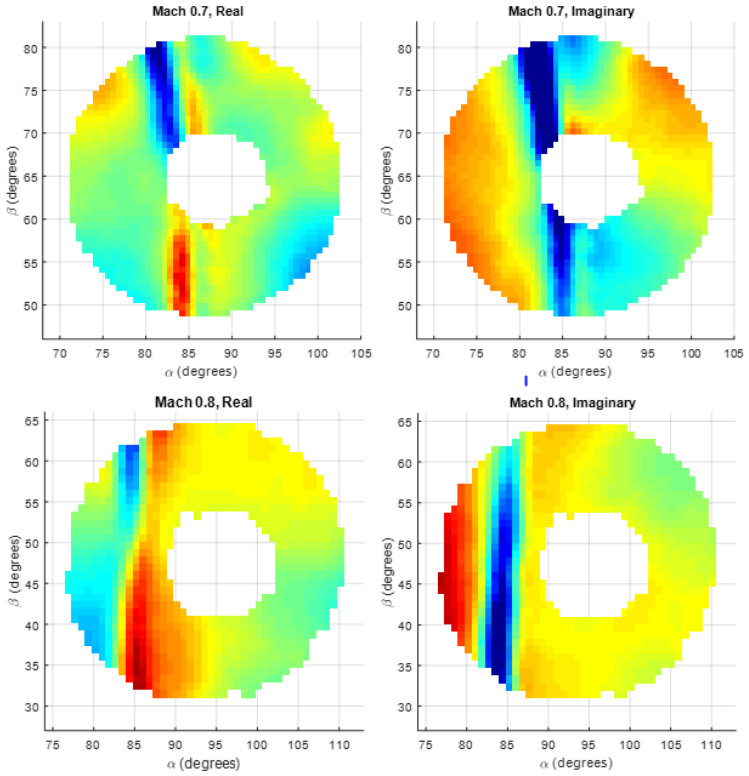

Figure 6: The real (left) and imaginary (right) parts of the DMD modes near St_D = 0.15 for Mach 0.7 and 0.8.

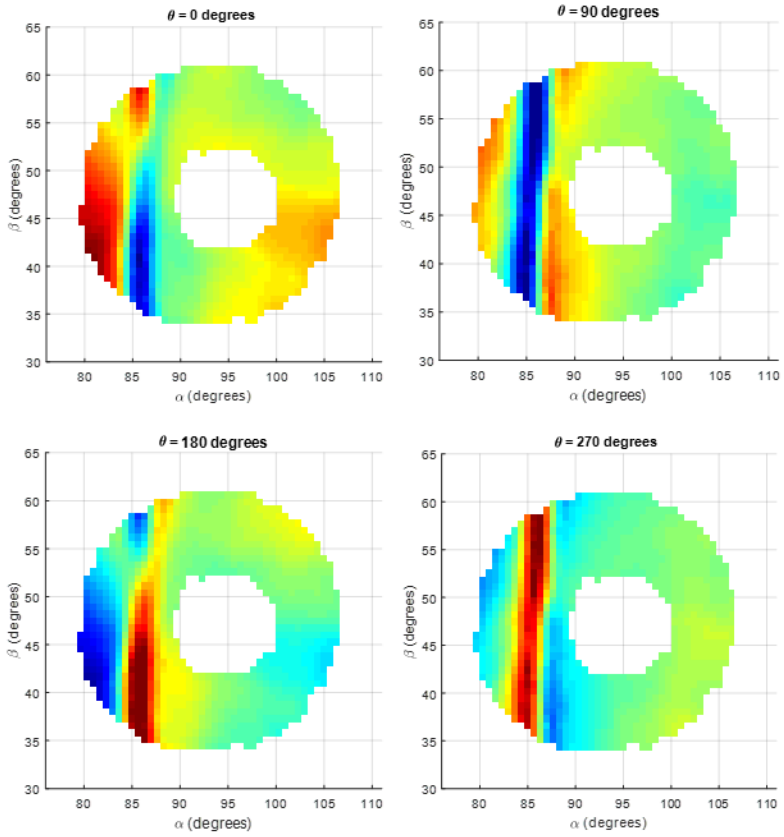

Figure 7: Reconstructed dominant DMD modes at St_D = 0.15 for Mach 0.8at phases 0, 90, 180, and 270 degrees.

Figure 7 shows the reconstructed temporal evolution of the DMD mode for St_D = 0.15 at Mach 0.8 at phases 0, 90, 180, and 270 degrees. These phases are representative of the whole period of the DMD mode. The shock is located at the point of maximum positive slope, and the optical shock strength is defined as a change in OPD-amplitude, ΔOPD, across the shock. It is visible near 85 degrees as a sharp gradient between a blue region and red regions. One-dimensional slices at β = 52 degrees are also shown in Figure 8 for clarity. At phase θ = 0 degrees, the shock is weak and located around 87 degrees. As the phase increases the shock moves upstream and the shock intensity increases until θ = 180 degrees where ΔOPD is the highest. Then the shock continues moving upstream and weakens until θ = 270 degrees where the change in ΔOPD is small again and the shock is at the furthest upstream point around α = 83 degrees. Overall, the shock exhibits a predominantly upstream motion; a similar upstream motion was observed at lower speeds of Mach 0.63 and a simple dynamical model was proposed to explain this behavior [2].

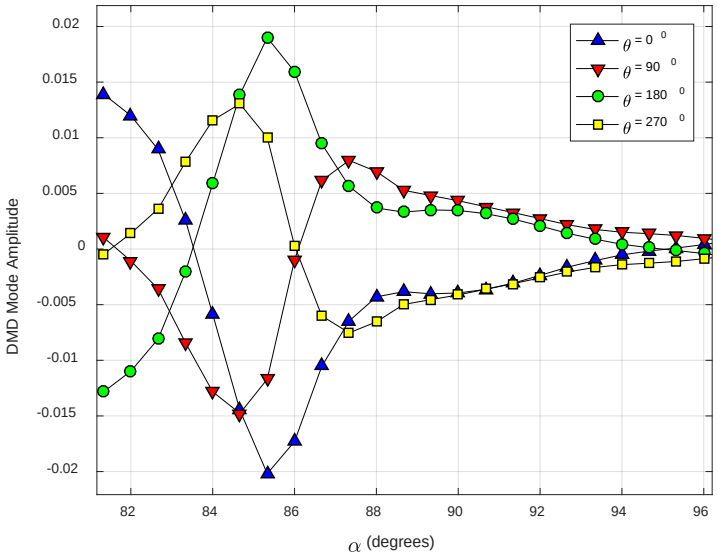

Figure 8: 1-D slices at β = 52 degrees of the DMD mode at St_D = 0.15 for Mach 0.8 phases shown in Figure 7.

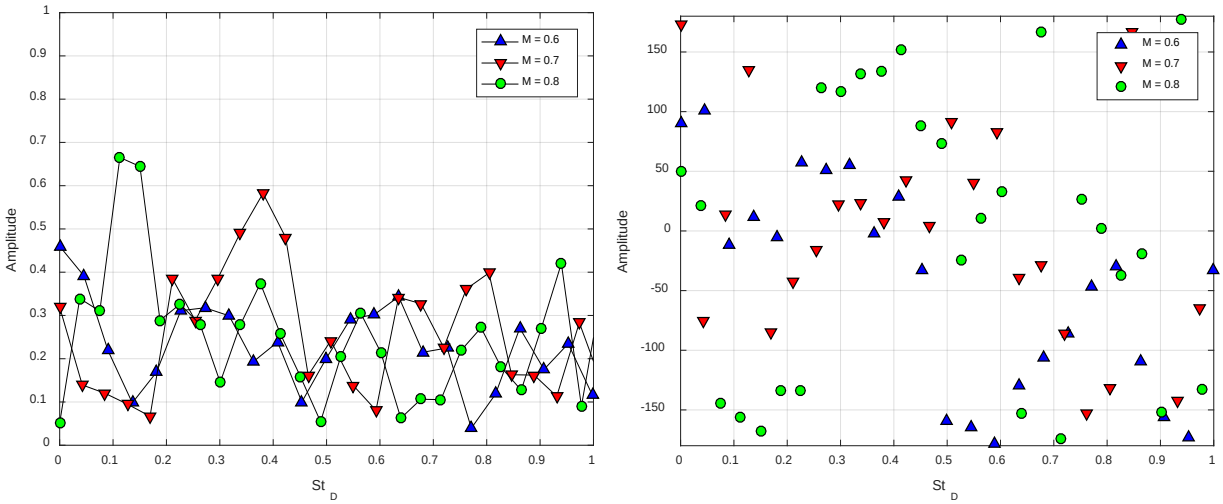

Figure 9: Normalized spectral correlation amplitude (left) and phase (right) between the DMD temporal coefficient at St_D = 0.15 and the wake pressure at location 3.

The DMD mode at StD = 0.15 at Mach numbers of 0.7 and 0.8 is clearly associated with the shock motion over the aperture. So it can be used to study the correlation between the shock motion and the pressures in the wake. Due to non-orthogonality of the DMD modes, one cannot treat individual c_k-coefficients as true temporal coefficients. One

way to extract a temporal evolution of a particular DMD mode is to project the DMD onto the original wavefronts, similar to how it is done for POD, $a_{DMD}(t) = \int OPD(x,y,t)\phi(x,y;f)dxdy$. The temporal coefficients of the DMD mode for St_D = 0.15 at Mach 0.7 and 0.8, given in Figure 6, were computed by projecting the mode onto the original wavefronts, and these coefficients were correlated with the all pressure sensors in the wake. Results of the spectral correlation with Sensor 3 for Mach 0.6 – 0.8 are shown in Figure 9. Sensor 3 was chosen for this analysis, as it had the highest correlations with the temporal coefficients, compared to other sensors. At Mach 0.6 there is no significant correlation, but there is strong correlation at St_D = 0.4 for Mach 0.7, shown in Figure 10, left. The phase of the correlation, shown in Figure 9, right, indicates that the shock motion is in phase with the pressure at Sensor 3. For Mach 0.8, the correlation is the highest at St_D = 0.15 and the shock motion is approximately 180 degrees out-of-phase with the pressure at this frequency. It is not quite clear at this moment why the phase switches from 0 to 180 degrees. One possibility is that the wake dynamics is different at Mach 0.7 and 0.8 due to a progressively stronger shock affecting the wake at Mach 0.8. Another possibility is that the unsteady shock creates some traveling structures at the separation line and it takes some time for them to convect downstream and affect the pressure in the wake, resulting in a different phase delay.

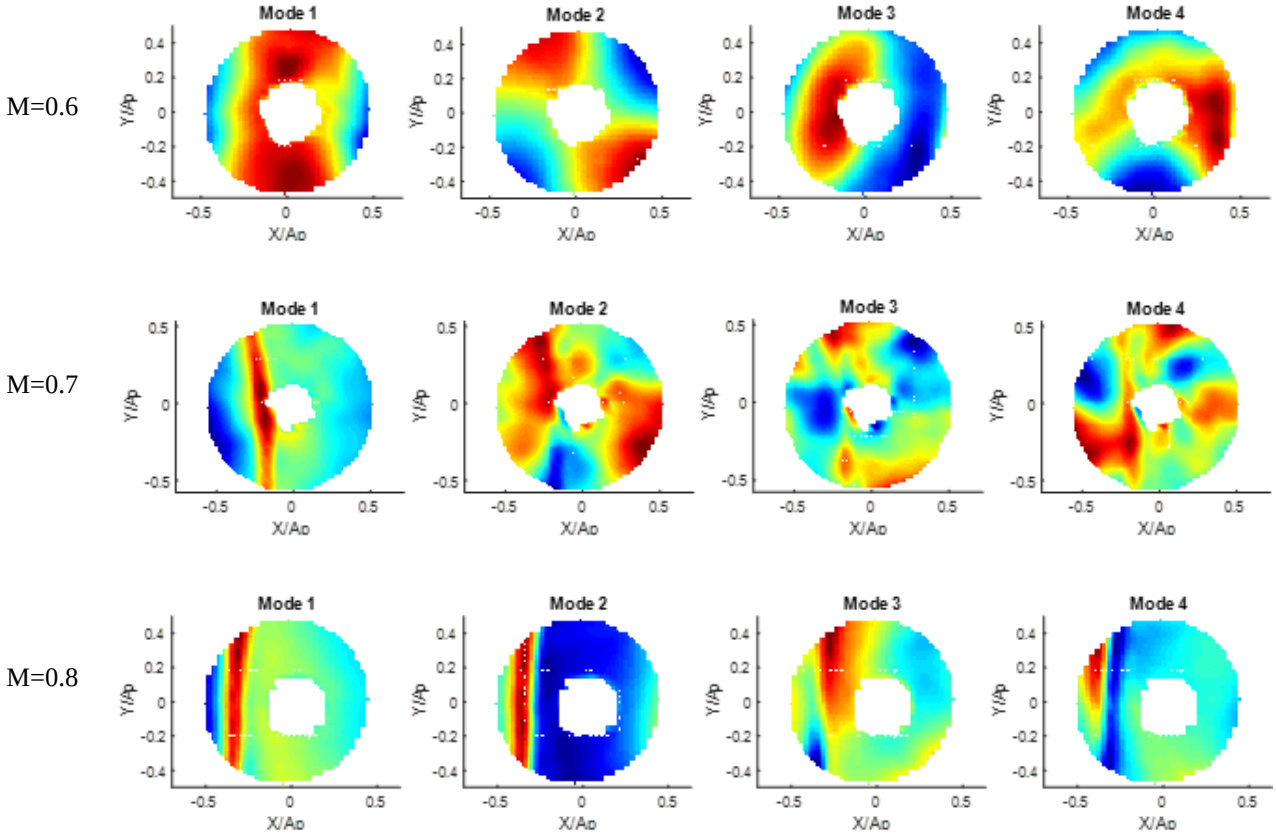

Figure 10: First 4 wavefront POD modes for M=0.6, 0.7 and 0.8. The viewing angle, α, is between 90 and 100 degrees. Flow goes from left to right.

Figure 10 shows the first four wavefront POD modes for Mach numbers of 0.6, 0.7 and 0.8 for wavefront sequences, collected at similar side-looking angles of α between 90 and 100 degrees. POD modes for Mach 0.5 are very similar to the ones for Mach 0.6 and are not presented in Figure 10. For all Mach numbers the first four modes contain more than 60% of the optical energy, see Figure 11, right; the first 20 POD modes contain about 90% of the optical energy. The first POD mode contains more energy at highest Mach number of 0.8 than for lower Mach numbers, see Figure 11, left. For Mach 0.6, the shock is very weak, and not visible on the aperture. At this angle, the flow is attached at subsonic Mach numbers and most of the density variations are due to the global flow adjustments

to the bulk motion of the separated wake downstream of the turret via Biot-Savart mechanism. For Mach 0.7 and 0.8 the first POD mode has a similar sharp discontinuity related to the presence of the unsteady shock. The shock presence is also evident in higher POD modes at Mach 0.8. At this speed, the shock is stronger and creates large unsteady distortions in the wavefronts, so the first POD modes primarily reflect the shock-related optical distortions. The shock-related effects can be also seen to some degree at Mach 0.7, but not as evident as for Mach 0.8.

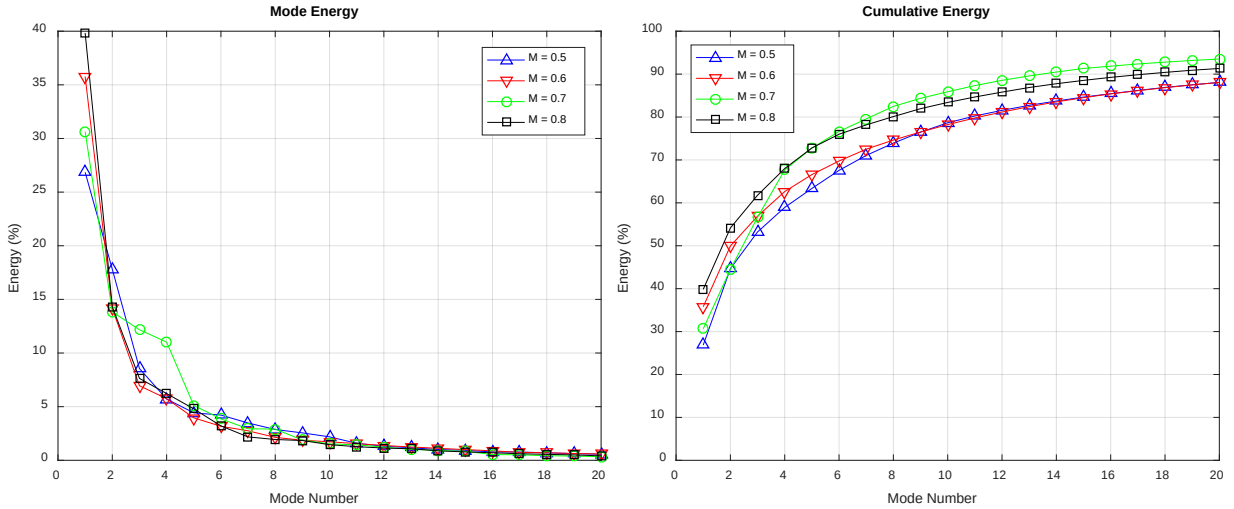

Figure 11: Energy in each POD mode (left), and cumulative energy (right) for all Mach numbers.

Figure 12 shows the power spectra for the temporal coefficients of the first two POD modes. For Mode 1, all Mach numbers have a peak near the separation line frequency of $St_D \sim 0.2$, but the Mach 0.6 the spectrum has much less energy, because the shock strength is very weak. The spectrum for Mach 0.7 has a peak around $St_D = 0.3$, while the spectrum for Mach 0.8 has a broader peak centered around $St_D = 0.2$. The spectra for all Mach numbers have a similar amount of energy for mode 2, but the spectrum for Mach 0.7 has a double peak at $St_D = 0.15$ and 0.3, and the spectrum for Mach 0.8 has only a broader one. Overall, the spectra features for all Mach numbers are similar to DMD power spectra presented in Figure 5.

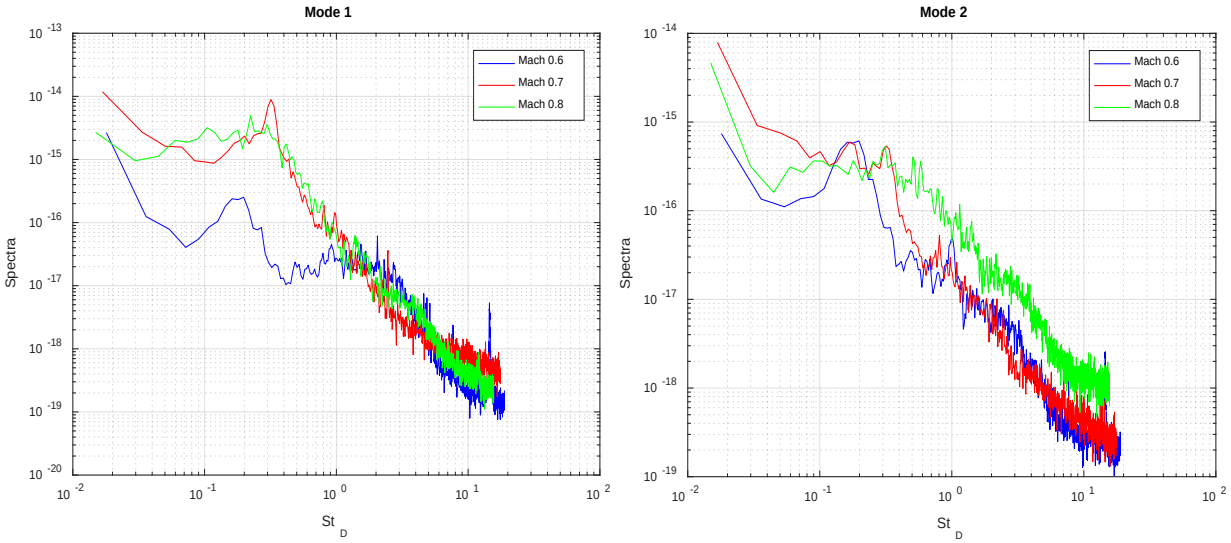

Figure 12: Power spectra of the POD temporal coefficients of Mode 1 (left) and Mode 2 (right) for Mach 0.6 – 0.8.

Figure 13 shows the power spectra for selected Sensors 3 and 6 at different Mach numbers. As Sensors 3 and 6 are located approximately at the same spanwise distance away from the centerline on both sides of the wake in the local flow frame of reference, the spectra at the same Mach number are expected to be similar; indeed, that is the case,

as it can be seen in Figure 13. Spectra for Sensor 3 and 6 have no peak frequency at the subsonic case, Mach 0.5, but at transonic speeds develop a peak at St_D = 0.3 for Mach 0.7, which shifts to St_D = 0.2 at Mach 0.8. The shift to a lower frequency at higher transonic Mach number was already observed in the shock motion in Figure 12 and in other experiments [3,19]. This shift in the wake pressure spectra toward the shock-related frequency indicates an increased coupling between the shock and the recirculation region downstream of the turret [3], resulting in spectral changes in the wake pressure. Similar conclusions that the shock is coupled with the wake were made in [22], where the shock motion was found to be correlated with the size of the recirculation region.

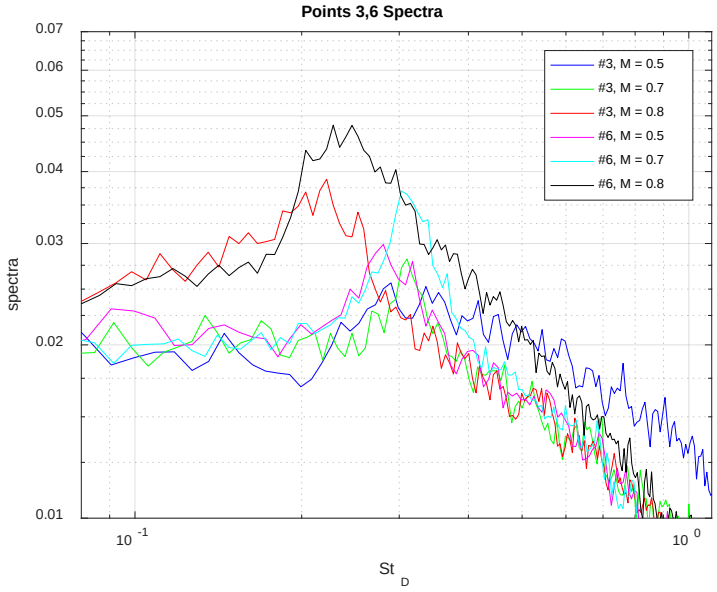

Figure 13: Power spectra of pressure Sensors 3 and 6 for different Mach number.

In order to study the correlation between the wavefronts at side-looking angles and the pressure field in the wake, temporal coefficients of the first two optical POD modes were correlated with the pressures at different locations in the wake. Modes 1 and 2 contain around 40-50% of the optical energy and were correlated with pressure for Sensor 3, see Figure 14. As it was mentioned before, the shock has been shown to move at a higher frequency at lower Mach numbers, and to shift down to St_D = 0.15 at higher Mach numbers due to the shock-wake coupling [21]. The correlation between the first POD mode and the Sensor 3, Figure 14, shows a similar trend, as for Mach 0.7 the correlation is the highest at St_D = 0.3 for Mach 0.7 and for Mach 0.8 the largest correlation shifts to St_D = 0.15. Note that the peak at St_D = 0.3 still exists for Mach 0.8, but gets weaker compared to Mach 0.7 case. As the first POD mode for Mach 0.7 and 0.8 looks very similar to the dominant DMD mode, shown in Figure 6, the correlations between the POD mode and pressures, Figure 14, top, look similar to the correlations between the DMD and pressures, Figure 9. As there is no shock present at Mach 0.6, the correlation between the first POD mode and the pressure in the wake is fairly week, below 0.3. It indicates that in transonic speeds the unsteady shock has a coupling or regularization effect on the pressure field in the wake. For Mode 1 at Mach 0.7 and 0.8 the correlations have roughly the same phase around 90 degrees over a range of frequencies St_D = 0.2..0.4; a similar trend in phase was observed in Figure 9 for the same frequency range. The correlation phase for Mach 0.8 near St_D = 0.1 shifts to 150 degrees, also consistent with the same phase shift, observed in Figure 9.

The correlation between the second POD mode and Sensor 3 also shows a strong peak at St_D = 0.3 for Mach 0.7, but the correlation is weaker for Mach 0.8, with a main peak shifting to about St_D = 0.1; the correlation is generally weak at lower Mach number of 0.6. The phase of the correlation shows more scatter in the range of St_D = 0.1..0.4, consistent with a generally weaker correlation, compared to the correlation with Mode 1.

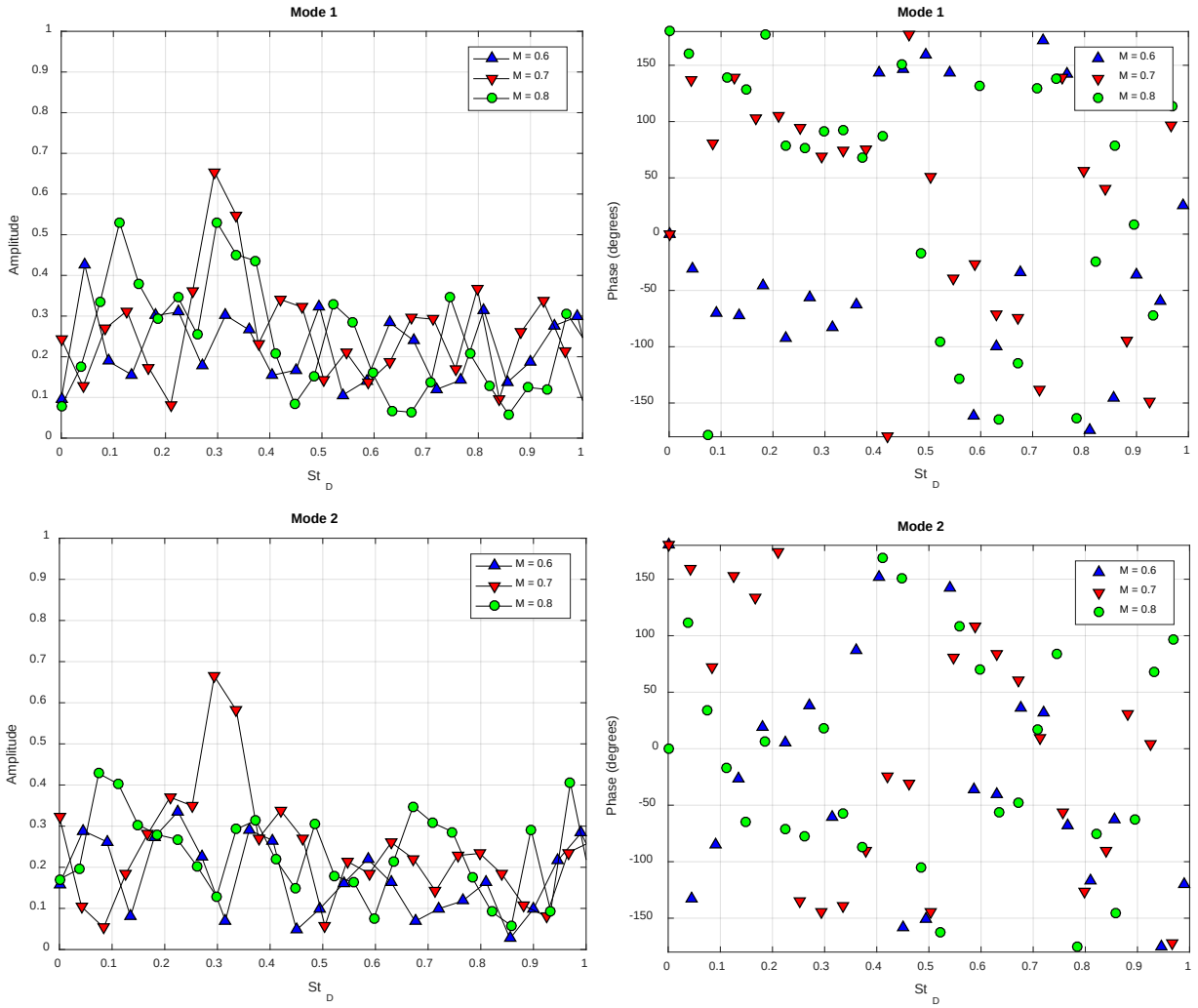

Figure 14: Normalized spectral correlation between the wavefront POD coefficients for Modes 1 and 2, and pressure Sensor 3 for Mach 0.6 – 0.8. Amplitude is shown on the left and the phase is depicted on the right.

V. Conclusions

Simultaneous aero-optical and pressure measurements were performed on a hemisphere in flight for Mach numbers from 0.5 – 0.8. Aero-optical measurements were collected over the aperture positioned near the apex of the turret and several unsteady pressure sensors were placed at the aircraft surface downstream of the turret inside the recirculation region downstream of the turret near the re-attachment point. Spatially-temporally resolved optical distortions were analyzed to capture the shock dynamics over the aperture in transonic flow. The shock was found to have an average location of α = 85 degrees, and to move approximately between α = 82 and 88 degrees.

The aero-optical distortions over the aperture were decomposed into dominant modes using DMD and POD techniques. Analysis of the both DMD and POD power spectra had shown that dynamic optical features are primarily present of the range of low frequencies, between St_D of 0.1 and 0.4. This range was associated with the unsteady separation motion in previous studies. Analysis of the dominant DMD mode at St_D = 0.15 at Mach number of 0.8 has revealed a predominantly upstream motion of the shock, when the shock appears near α = 88 degrees, grows in strength and moves upstream until it reaches α = 84 degrees. After that, the shock strength starts decreasing and the shock disappears around α = 82 degrees. For M = 0.7 the shock, appearing over the aperture, is strong enough to enhance or amplify specific frequencies around St_D = 0.2; however, this amplification disappears at a higher Mach number of 0.8, where both DMD and POD spectra have a broad "hump" near St_D = 0.2. Temporal coefficients related to dominant DMD and POD modes were calculated and correlated with each individual pressure sensor in the wake. The largest

correlations were found between the optical distortions and pressure sensors, located on sides of the wake in the spanwise direction. Analysis of the spectral correlations between these pressure sensors and the temporal coefficients of the dominant DMD or POD modes had revealed that the normalized correlations have high, with a value of around 0.5, near St_D = 0.3-0.4 for Mach number of 0.7, as well as at a lower frequency of St_D = 0.2 for Mach number of 0.8. The wake is mostly uncorrelated with the optical distortions at Mach number of 0.6, indicating that in transonic speeds the unsteady shock has a regularization effect on the pressure field in the wake.

The increased correlation between wake pressure and aero-optical distortions near the shock-related frequency for the first two POD modes at transonic speeds indicates that the wake surface pressure might be used to estimate optical distortions due to the shock. This could be beneficial because pressure data can be analyzed more quickly than optical wavefronts for adaptive optics control loops, avoiding latency issues and a need for cooperative target. In the future work, downstream pressure measurements will be used in attempt to predict aero-optical distortions over the aperture.

Acknowledgments

This work is supported by the Joint Technology Office, Grant number FA9550-13-1-0001. The U.S. Government is authorized to reproduce and distribute reprints for governmental purposes notwithstanding any copyright notation thereon.

References

[1] S. Gordeyev and E. Jumper, “Fluid Dynamics and Aero-Optics of Turrets”, *Progress in Aerospace Sciences*, **46**, (2010), pp. 388-400.

[2] N. De Lucca, S. Gordeyev and E.J. Jumper, "In-flight aero-optics of turrets”, *Journal of Optical Engineering*, **52**(*7*), 071405, 2013.

[3] J. Morrida, S. Gordeyev, N. De Lucca, E.J. Jumper, “Shock-Related Effects on Aero-Optical Environment for Hemisphere-On-Cylinder Turrets at Transonic Speeds,” *Applied Optics*, **56**(*16*), pp. 4814-4824, 2017.

[4] S. Gordeyev, A. Vorobiev, E. Jumper, S. Gogineni and D.J. Wittich, “Studies of Flow Topology around Hemisphere at Transonic Speeds Using Time-Resolved Oil Flow Visualization”, AIAA Paper 2016-1459, 2016.

[5] C. Porter, S. Gordeyev, M. Zenk and E. Jumper, "Flight Measurements of the Aero-Optical Environment around a Flat-Windowed Turret”, *AIAA Journal*, **51**(*6*), pp. 1394-1403, 2013.

[6] J. Morrida, S. Gordeyev, E. Jumper, “Transonic Flow Dynamics Over a Hemisphere in Flight”, AIAA Paper 2016-1349, 2016.

[7] D. J. Goorskey, R. Drye and M. R. Whiteley, “Dynamic modal analysis of transonic Airborne Aero-Optics Laboratory conformal window flight-test aero-optics”, *Journal of Optical Engineering*, **52** (7), 071414, 2013.

[8] E.J. Jumper, S. Gordeyev, D. Cavalieri, P. Rollins, M.R. Whiteley and M.J. Krizo, “Airborne Aero-Optics Laboratory - Transonic (AAOL-T),” AIAA Paper 2015-0675, 2015.

[9] E.J. Jumper, M. Zenk, S. Gordeyev, D. Cavalieri and M.R. Whiteley, "Airborne Aero-Optics Laboratory”, *Journal of Optical Engineering*, **52**(*7*), 071408, 2013.

[10] A. Vorobiev, S. Gordeyev, E. Jumper, S.Gogineni, A. Marruffo and D.J. Wittich, “ Low-Dimensional Dynamics and Modeling of Shock-Separation Interaction over Turrets at Transonic Speeds,” AIAA Paper 2014-2357, 2014.

[11] W.R. Burns, S. Gordeyev, E. Jumper, S. Gogineni, M. Paul and D.J. Wittich, “ Estimation of Aero-Optical Wavefronts Using Optical and Non-Optical Measurements ”, AIAA Paper 2014-0319, 2014.

[13] A. Nightingale, B. Goodwine, M. Lemmon, and E. Jumper, “Phase-Locked-Loop Adaptive-Optic Controller and Simulated Shear Layer Correction”, *AIAA Journal*, **51**(*11*), pp. 2714-2726, 2013.

[14] D. Duffin, “Feed-Forward Adaptive-Optic Correction of a Weakly-Compressible High-Subsonic Shear Layer”, PhD Thesis, University of Notre Dame, 2009.

[15] J. Morrida, S. Gordeyev, N. De Lucca, E. Jumper. “Aero-Optical Investigation of Transonic Flow Features and Shock Dynamics on Hemisphere-On-Cylinder Turrets”, AIAA Paper 2015-0676, 2015.

[16] P.J. Schmid. "Dynamic mode decomposition of numerical and experimental data." *Journal of Fluid Mechanics*, **656**, pp. 5–28, 2010.

[17] K. Taira, S.L. Brunton, S.T.M. Dawson, C.W. Rowley, T. Colonius, B.J. McKeon, O.T. Schmidt, S. Gordeyev, V. Theofilis, L.S. Ukeiley, “Modal Analysis of Fluid Flows: An Overview”, to appear in AIAA Journal, 2017.

[18] F. Richecoueur, L. Hakim, A. Renaud, L. Zimmer, "DMD Algorithms for Experimental Data Processing in Combustion", Center for Turbulence Research, Summer Proceedings, 2012.

[19] Goorskey D., Drye R. and Whitely M., "Dynamic Modal Analysis of Transonic Airborne Aero-Optics Laboratory Conformal Window Flight-Test Aero optics," *Journal of Optical Engineering,* **52**(*7*), 071414, 2013.
[20] S. Gordeyev, N. De Lucca, E. Jumper, K. Hird, T.J. Juliano, J.W. Gregory, J. Thordahl and D.J. Wittich, "Comparison of Unsteady Pressure Fields on Turrets with Different Surface Features using Pressure Sensitive Paint", *Experiments in Fluids*, **55**, p. 1661, 2014.
[21] N. De Lucca, S. Gordeyev, and E. Jumper, "Global Unsteady Pressure Fields Over Turrets In-Flight", AIAA Paper 2015-0677, 2015.
[22] S.J. Beresh, J.F. Henfling, R.W. Spillers, B. O.M. Pruett, "Unsteady Shock Motion in a Transonic Flow over a Wall-Mounted Hemisphere", AIAA Paper 2013-3201, 2013.